Annals of the University of Bucharest (mathematical series)
4 (LXII) (2013), 141–154

Redundancy and inversion of the Compton transform

Voichita Maxim

Abstract - Data acquired with a Compton gamma-camera are empirical measures of the Compton transform. This integral transform consists to calculate integrals of the intensity distribution of the source on conical surfaces. In this work, we analyze the direct problem and we show that under the non-realistic hypothesis of an infinite extent detector it is possible to isolate classes of Compton projections that are related together via the Radon transform. A reduction of dimensionality may be operated in the data space, leading to a new transform that reveals to be invertible. The invertibility of the Compton transform follows as a consequence and takes the form of a particular filtered backprojection tomographical reconstruction formula. In practical situations where the acquired data allows a rather poor estimation of the Compton projections, averaging projections that belong to the same class allows to reduce the noise in the reconstructed images. In the case of a finite extent camera, numerical experiments show that the reconstructed images present artifacts due to absence of data in some projections. Selection of non-truncated projections may be a way to partially get around this issue.

Key words and phrases : integral transform, filtered backprojection, Compton transform, Compton gamma-camera, medical imaging, SPECT.

Mathematics Subject Classification (2010) **:** 65R10, 65R32, 65Z05, 92C55.

1. Introduction

The electronically collimated camera, or Compton camera, is a gamma-ray detection system initially developed for imaging sources in the energy range of 1–30 MeV and was used in astronomy. First introduced into nuclear medicine imaging in 1974 by Todd and Nightingale [14], the concept benefits of a renewal of interest due to recent advances in electronics and to increase in computing power. Several groups in the world actively work on various aspects of this mode of imaging. The benefits that it may bring are investigated in astronomy (see, e.g. [2]), nuclear medicine (e.g. [6, 5]), security and nuclear nonproliferation (e.g. [8]).

At the date, the most widely used image reconstruction algorithms for the Compton camera are iterative, generally List-Mode Maximum Likelihood Expectation Maximization algorithms. In 1994, Cree and Bones [4]

developed an analytic algorithm for photons scattered in the direction orthogonal to the first detector. Although this limitation balance out the benefits of the imaging device, the method has the merit to be the first analytical reconstruction method and also to show that in the case of an infinite extent parallel-plate Compton camera, a properly chosen subset from the set of data suffices to reconstruct the image. Methods consisting to transform the Compton projections in either 3D Radon projections or line projections were proposed afterwards by several authors. Some of them, e.g. [3, 11, 7], relate on spherical harmonics series decomposition. The Hilbert transform may also be used for the same purpose. In [12], B. Smith developed two reconstruction methods corresponding to two usual models of the Compton projections. Further, a discussion of the completeness conditions is carried and suggestions about the ideal geometry are made in [13].

A central-slice theorem for the inversion of the Compton transform was given by Maxim et al in [10]. Further developments reported in [9] lead to a filtered backprojection expression facilitating the computer implementation.

This work is taking further the results from [10] and [9]. It gives a new formulation of the direct problem and analyzes the redundant structure in the model of the data. The reconstruction method, based on a filtered backprojection formulation of the inverse transform, allows several slightly different data aggregation or selection procedures and thus possibly an amelioration of the signal-to-noise ratio for real data. The paper is organised as follows. Section 2 presents the functioning principle of the Compton camera and the model considered afterwards for the Compton projections. Classes of projections that are related together via the Radon transform are defined in section 3 and a method for the inversion of the Compton transform is proposed in section 4. Section 5 is devoted to numerical tests in a realistic setup, where a finite extent camera with finite spatial and energy resolution was simulated with the Monte-Carlo simulation tool MEGAlib [15], based on Geant4 [1]. Finally, section 6 draws some conclusions from the study.

2. Direct Compton transform

A Compton camera is composed of two position and energy sensitive detectors. The first one, called the scatter detector, is designed to produce with high probability the Compton scattering of an incident γ ray. It also has low photoelectric absorption probability. The second detector, called the absorption detector, is designed to have a high photoelectric absorption probability. If the energy of the incoming ray is E_0 and the energy transmitted to the electron in the scattering process is E_1, the Compton scattering angle $\beta \in [0, \pi]$ may be calculated by energy conservation as

$$\cos\beta = 1 - \frac{m_e c^2 E_1}{(E_0 - E_1)E_0}\,, \tag{2.1}$$

where $m_e c^2$ is the energy of an electron at rest. The direction of the scattered γ ray, as measured by the position sensitive detectors, along with the Compton angle confine the possible incoming path of the initial γ ray to the surface of a cone of half-opening angle β, called hereafter the Compton cone.

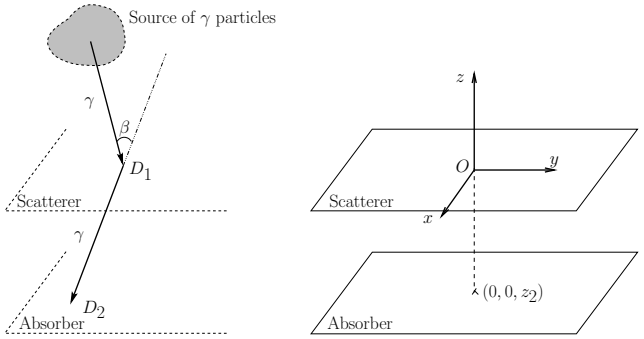

(a) (b)

Figure 1: Principle of the Compton camera detection (a) and positioning of the direct frame $Oxyz$ (b).

We place the origin of an orthogonal coordinate system $Oxyz$ at the center of the scatter detector, with the Oz axis orthogonal to the detectors, oriented such that the absorber is located at a depth $z_2 < 0$.

A recorded event corresponds to a γ particle interacting first in the scatterer, at a point $D_1(x_1, y_1, 0)$, then in the absorber, at a point $D_2(x_2, y_2, z_2)$. We denote respectively α and δ the polar angle and the azimuth of the vector $\overrightarrow{D_2D_1}$ giving the direction of the axis of the Compton cone. After normalisation, the same vector may be represented as:

$$\Omega(\alpha, \delta) = (\sin\alpha\cos\delta, \sin\alpha\sin\delta, \cos\alpha). \tag{2.2}$$

The equation of a Compton cone of apex $u = (x, y, z)$, half-opening angle β and axis directed by $\Omega(\alpha, \delta)$ is:

$$v \in \mathbb{R}^3, \quad (v - u).\Omega(\alpha, \delta) = \|v - u\|_2 \cos\beta. \tag{2.3}$$

The acquisition process with a Compton gamma-camera is related to a particular integral transform, the Compton transform ([10]) and to Compton projections:

Definition 2.1. *The Compton transform $\mathscr{C}$ maps a function on $\mathbb{R}^3$ into the set of its weighted integrals over conical surfaces. More specifically, if $\alpha \in [0, \pi], \delta \in]-\pi, \pi]$ and $\beta \in [0, \pi]$, the Compton projection $\mathscr{C}_{\alpha,\delta,\beta}$ associates to*

a function $f \in \mathscr{S}(\mathbb{R}^3)$, the Schwartz space, the application $\mathscr{C}_{\alpha,\delta,\beta} f : \mathbb{R}^3 \to \mathbb{R}$ defined by

$$\begin{aligned} \mathscr{C}_{\alpha,\delta,\beta} f(u) &= \int_{(v-u).\Omega(\alpha,\delta)=\|v-u\|_2 \cos\beta} f(v) \cos\theta dv \\ &= \int_{(v-u).\Omega(\alpha,\delta)=\|v-u\|_2 \cos\beta} f(v) \frac{z}{\|v-u\|_2} dv, \end{aligned} \tag{2.4}$$

where $v = (x, y, z)$ is a vector from $\mathbb{R}^3$, θ is the polar angle of the vector $v - u$ and $\Omega(\alpha, \delta) = (\sin\alpha\cos\delta, \sin\alpha\sin\delta, \cos\alpha)$.

When a source of γ particles having intensity distribution represented by a function $f : \mathbb{R}^3 \to \mathbb{R}$ is observed by a Compton camera, the fraction of events recorded with parameters $(u, \alpha, \delta, \beta)$ is proportional to $\mathscr{C}_{\alpha,\delta,\beta} f(u)$, which is the integral of f, weighted by a factor accounting for the efficiency of the camera at different incidence angles, on the surface of the Compton cone with apex u, axis directed by $\Omega(\alpha, \delta)$ and half-opening angle β. A Compton camera having an infinite extent planar scatterer at $z = 0$ (as the one represented in figure 1), measures Compton projections $\mathscr{C}_{\alpha,\delta,\beta} f(u)$ for all $u = (x_1, y_1, 0) \in \mathbb{R}^2 \times \{0\}$.

Let (e_1, e_2, e_3) be the standard basis of $\mathbb{R}^3$. The vectors $d_1 = (\cos\delta, \sin\delta, 0)$, $d_2 = (-\sin\delta, \cos\delta, 0)$ and e_3 also form an orthonormal basis of $\mathbb{R}^3$, defining a reference frame $Otsz$ obtained by rotation of $Oxyz$ about the Oz axis.

Let us consider a Compton cone that intersects each plane $z = z_0$ upon an ellipse, as in figure 2. This constrain may also be expressed by the equation $\sin^2\beta < \cos^2\alpha$. When $\alpha, \beta \in [0, \pi/2)$, an equivalent formulation is

$$\alpha + \beta < \pi/2. \tag{2.5}$$

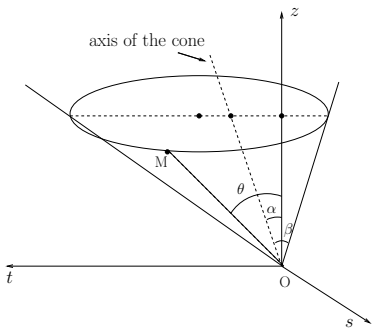

Figure 2: The intersection between the Compton cone and a plane $z = z_0$ is an ellipse with its major axis parallel to Ot.

Let us define:

$$a(\alpha,\beta) = \frac{\sin\beta\cos\beta}{\cos^2\alpha-\sin^2\beta}, \tag{2.6}$$

$$b(\alpha,\beta) = \frac{\sin\beta}{\sqrt{\cos^2\alpha-\sin^2\beta}}, \tag{2.7}$$

$$c(\alpha,\beta) = \frac{\sin\alpha\cos\alpha}{\cos^2\alpha-\sin^2\beta}. \tag{2.8}$$

Lemma 2.1. *For some $\alpha,\beta\in[0,\pi/2)$ verifying $\alpha+\beta<\pi/2$ and some $\delta\in(-\pi,\pi]$, the Compton projection $\mathscr{C}_{\alpha,\delta,\beta}f$ of a function $f\in\mathscr{S}(\mathbb{R}^3)$, at a point of coordinates $(x_1,y_1,0)=td_1+sd_2$, may be expressed as*

$$\mathscr{C}_{\alpha,\delta,\beta}f(td_1+sd_2)=b(\alpha,\beta)\int_0^\infty\int_0^{2\pi} f((t+zc(\alpha,\beta)+za(\alpha,\beta)\cos\varphi)d_1 \\ +(s+zb(\alpha,\beta)\sin\varphi)d_2+ze_3)zd\varphi dz. \tag{2.9}$$

Proof. For some given $z_0>0$, the intersection of the cone having the apex at $(0,0,0)$ and angular parameters (α,δ,β), with the plane $z=z_0$ is described by the equation

$$(t(\cos^2\alpha-\sin^2\beta)-z_0\sin\alpha\cos\alpha)^2+s^2\cos^2\beta(\cos^2\alpha-\sin^2\beta)=z_0^2\sin^2\beta\cos^2\beta, \tag{2.10}$$

when $\cos\alpha\neq\sin\beta$, and by

$$-2tz_0\sin\alpha\cos\alpha+s^2\cos^2\beta=z_0^2(\sin^2\beta-\cos^2\beta) \tag{2.11}$$

otherwise. For $\alpha,\beta\in[0,\pi/2)$ such that $\alpha+\beta<\pi/2$, the intersection is an ellipse. Its major and minor axes equal $z_0a(\alpha,\beta)$ and $z_0b(\alpha,\beta)$, respectively. The distance from the center of the ellipse to the axis Oz equals $z_0c(\alpha,\beta)$. One possible parametric representation of the Compton cone in the case $\alpha+\beta<\pi/2$ is then:

$$\begin{cases} t=z\dfrac{\sin\alpha\cos\alpha}{\cos^2\alpha-\sin^2\beta}+ & z\dfrac{\sin\beta\cos\beta}{\cos^2\alpha-\sin^2\beta}\cos\varphi \\ s= & z\dfrac{\sin\beta}{\sqrt{\cos^2\alpha-\sin^2\beta}}\sin\varphi \\ z=z & \end{cases}, \quad z\geq 0,\ \varphi\in(-\pi,\pi]. \tag{2.12}$$

Consequently, the equation of a cone with apex $t_0d_1+s_0d_2$ is:

$$\begin{cases} t=t_0+zc(\alpha,\beta) & +za(\alpha,\beta)\cos\varphi \\ s=s_0 & +zb(\alpha,\beta)\sin\varphi \\ z=z & \end{cases}, \quad z\geq 0,\ \varphi\in(-\pi,\pi]. \tag{2.13}$$

The result of the lemma follows from (2.4) and (2.13). □

The purpose of our method is to determine from the data the values of the unknown function f, by inverting the Compton transform (2.9). Note that the problem is overestimated since the image lies in a three dimensional space whereas the data lie in a five dimensional space. Of course this redundancy in the data is conditioned by the non realistic assumption that the detectors are of infinite area. Results reported in [4] show that the image of the source can be reconstructed from only projections having the parameter α set to zero. Incidentally, note that when $\alpha = 0$ the parameter δ has no meaning and the inversion is done in this case from a three dimensional space to another three dimensional space. In the following section, we give a new insight of the method proposed in [10], method that allows to reconstruct the image of the source when all the projections, for some given value of α in the range $\left[0, \frac{\pi}{2}\right)$, are known.

A different approach, consisting to gather in a projection all the surface integrals on cones having a common apex and symmetry axis, was adopted in [3, 11, 7, 12, 13]. The objective in this case is to calculate either Radon projections on planes or cone-beam projections that can then be exploited by an other image reconstruction algorithm.

3. Inversion of the Compton transform

For some given parameters α, δ, β verifying the constraints described in the previous section and for a planar scatterer, the Compton projection $\mathscr{C}_{\alpha,\delta,\beta} f$ may also be seen as a function of $(u_1, u_2) \in \mathbb{R}^2$. The two-dimensional Radon transform along a direction $\Delta = (\cos\delta, \sin\delta)$ of a function $g : \mathbb{R}^2 \to \mathbb{R}$ is given by:

$$\mathscr{R}_\delta g(s) = \int_{v.\Delta=s} g(v)dv = \int_{-\infty}^{\infty} g(s\Delta + t\Delta^\perp)dt, \tag{3.1}$$

where $\Delta^\perp = (-\sin\delta, \cos\delta)$ is orthogonal to Δ.

For f, real-valued function defined on $\mathbb{R}^3$, and for $z \in \mathbb{R}$, let $f_z : (x, y) \in \mathbb{R}^2 \mapsto f(x, y, z)$ be the restriction of f to $\mathbb{R}^2$.

Proposition 3.1. *Let $\alpha, \beta \in [0, \pi/2)$ verifying $\alpha+\beta < \pi/2$ and $\delta \in (-\pi, \pi]$. For any $f \in \mathscr{S}(\mathbb{R}^3)$ we have:*

$$\mathscr{R}_{\delta+\frac{\pi}{2}} \mathscr{C}_{\alpha,\delta,\beta} f(s) = b(\alpha, \beta) \int_0^\infty \int_0^{2\pi} \mathscr{R}_{\delta+\frac{\pi}{2}} f_z(s + zb(\alpha, \beta)\sin\varphi) z d\varphi dz. \tag{3.2}$$

Proof. Applying the Radon transform along the direction $(-\sin\delta, \cos\delta)$ to

the Compton projection $\mathscr{C}_{\alpha,\delta,\beta}f$ gives:

$$\begin{aligned}\mathscr{R}_{\delta+\frac{\pi}{2}}\mathscr{C}_{\alpha,\delta,\beta}f(s) &= \int_{-\infty}^{\infty}\mathscr{C}_{\alpha,\delta,\beta}f(td_1+sd_2)dt \\ &= b(\alpha,\beta)\int_{-\infty}^{\infty}\int_0^{\infty}\int_0^{2\pi} f((t+zc(\alpha,\beta)+za(\alpha,\beta)\cos\varphi)d_1 \\ &\qquad +(s+zb(\alpha,\beta)\sin\varphi)d_2+ze_3)zd\varphi dzdt.\end{aligned} \tag{3.3}$$

After a permutation of the integrals we obtain:

$$\begin{aligned}&\mathscr{R}_{\delta+\frac{\pi}{2}}\mathscr{C}_{\alpha,\delta,\beta}f(s) \\ &\quad = b(\alpha,\beta)\int_0^{\infty}\int_0^{2\pi}\int_{-\infty}^{\infty} f((t+zc(\alpha,\beta)+za(\alpha,\beta)\cos\varphi)d_1 \\ &\qquad +(s+zb(\alpha,\beta)\sin\varphi)d_2+ze_3)zdtd\varphi dz.\end{aligned} \tag{3.4}$$

Equation (3.2) results now from (3.4) and the definition of the Radon transform. □

The right-hand side term of the equation (3.2) depends on α and β only through $b(\alpha,\beta)$, meaning that it gets the same value for all couples (α,β) such that $b(\alpha,\beta)$ equals to some given $\tau \geq 0$. When $b(\alpha,\beta)=\tau\geq 0$, either α or β can be calculated from (2.7) as function of the other parameter through the relation:

$$\tau\cos\alpha = \sqrt{1+\tau^2}\sin\beta, \tag{3.5}$$

since both applications $\beta\in\left[0,\frac{\pi}{2}-\alpha\right)\mapsto b(\alpha,\beta)\in\mathbb{R}_+$, for some given $\alpha\in\left(0,\frac{\pi}{2}\right)$, and $\alpha\in\left[0,\frac{\pi}{2}-\beta\right)\mapsto b(\alpha,\beta)\in\mathbb{R}_+$, for some given $\beta\in\left[0,\frac{\pi}{2}-\alpha\right)$, are one-to-one. For the instance, when $\alpha=0$ one gets $\tau=\tan\beta$.

It is then natural to define a new integral transform, that we will call hereafter $\mathscr{P}$, which is a Radon transform composed with a Compton transform.

Definition 3.1. *For some given $\tau\geq 0$ and $\delta\in(-\pi,\pi]$, the projection $\mathscr{P}_{\tau,\delta}f$ of a function $f\in\mathscr{S}(\mathbb{R}^3)$ is defined as:*

$$s\in\mathbb{R},\quad \mathscr{P}_{\tau,\delta}f(s)=\tau\int_0^{\infty}\int_0^{2\pi}\mathscr{R}_{\delta+\frac{\pi}{2}}f_z(s+z\tau\sin\varphi)zd\varphi dz. \tag{3.6}$$

Proposition 3.2. *For any given $\tau\geq 0$, $\delta\in(-\pi,\pi]$, $\alpha,\beta\in[0,\pi/2)$ verifying $\alpha+\beta<\pi/2$ and $b(\alpha,\beta)=\tau$, we have:*

$$\mathscr{P}_{\tau,\delta}=\mathscr{R}_{\delta+\frac{\pi}{2}}\mathscr{C}_{\alpha,\delta,\beta}. \tag{3.7}$$

Proof. The proof follows immediately from definition 3.1 and proposition 3.1. □

Equation (3.7) can be interpreted as a consistency condition for the Compton projections. A numerical illustration of this result is presented

in figure 3 for Compton projections calculated through equation (2.9). It shows the same projection $\mathscr{P}_{\sqrt{3},\pi/4}$ of a small spherical source with uniform intensity distribution, calculated both from the Compton projections $\mathscr{C}_{0,\frac{\pi}{4},\frac{\pi}{3}}$ and $\mathscr{C}_{\frac{\pi}{5},\frac{\pi}{4},\arcsin(\frac{\sqrt{3}}{2}\cos\frac{\pi}{5})}$.

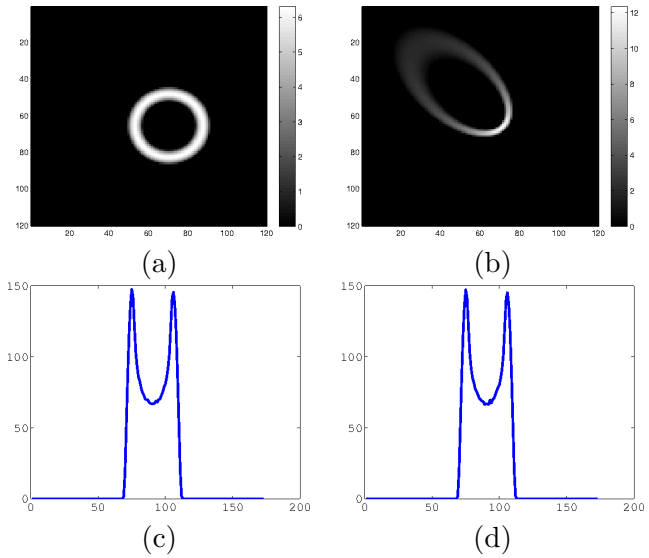

Figure 3: The same projection $\mathscr{P}_{\tau,\delta}$ may be calculated from any of an infinity of different Compton projections. On the top row, two Compton projection $\mathscr{C}_{\alpha,\frac{\pi}{4},\beta}$ of the same spherical source are presented. Image (a) was obtained for $\alpha = 0$ and $\beta = \pi/3$. Image (b) was obtained for $\alpha = \pi/5$, $\beta = \arcsin(\frac{\sqrt{3}}{2}\cos\frac{\pi}{5})$. For both images $b(\alpha,\beta) = \sqrt{3}$. In this simulation the projections were calculated exactly, from (2.9). Plots (c) and (d) on the bottom row represent the Radon projections of angle $\delta + \frac{\pi}{2} = \frac{3\pi}{4}$ of, respectively, (a) and (b). The similarity between (c) and (d) is a consequence of (3.7).

Note that the $\mathscr{P}$ transform produces a data set included in a three dimensional space, indexed by $\tau \geq 0$, $\delta \in (-\pi,\pi]$ and $s \in \mathbb{R}$. The size of the minimally required data set can be further reduced, as shown by the following lemma.

Lemma 3.1. *For any given $\alpha,\beta \in [0,\pi/2)$, $\alpha+\beta < \pi/2$, and any given $\delta \in (-\pi,\pi]$ we have:*

$$\mathscr{R}_{\delta+\frac{\pi}{2}}\mathscr{C}_{\alpha,\delta+\pi,\beta} = \mathscr{R}_{\delta+\frac{\pi}{2}}\mathscr{C}_{\alpha,\delta,\beta}. \tag{3.8}$$

Proof. Let us consider a function $f \in \mathscr{S}(\mathbb{R}^3)$. Let $d_1' = (\cos(\delta+\pi),\sin(\delta+\pi))$ and $d_2' = (-\sin(\delta+\pi),\cos(\delta+\pi))$ be the opposite vectors to, respectively,

d_1 and d_2. Then

$$\begin{aligned}\mathscr{R}_{\delta+\frac{\pi}{2}}\mathscr{C}_{\alpha,\delta+\pi,\beta}f(s) &= \int_{-\infty}^{\infty}\mathscr{C}_{\alpha,\delta+\pi,\beta}f(td_1+sd_2)dt \\ &= \int_{-\infty}^{\infty}\mathscr{C}_{\alpha,\delta+\pi,\beta}f(-td_1'-sd_2')dt. \end{aligned} \tag{3.9}$$

From the expression of the Compton transform given by lemma 2.1 we get:

$$\begin{aligned}&\mathscr{R}_{\delta+\frac{\pi}{2}}\mathscr{C}_{\alpha,\delta+\pi,\beta}f(s) \\ &\quad= b(\alpha,\beta)\int_{-\infty}^{\infty}\int_0^{\infty}\int_0^{2\pi} f((-t+zc(\alpha,\beta)+za(\alpha,\beta)\cos\varphi)d_1' \\ &\qquad\qquad +(-s+zb(\alpha,\beta)\sin\varphi)d_2'+ze_3)zd\varphi dzdt.\end{aligned} \tag{3.10}$$

Integrating first on t and applying the definition of the Radon transform leads to:

$$\mathscr{R}_{\delta+\frac{\pi}{2}}\mathscr{C}_{\alpha,\delta+\pi,\beta}f(s) = \int_0^{\infty}\int_0^{2\pi}\mathscr{R}_{\delta+\frac{\pi}{2}}f_z(s-zb(\alpha,\beta)\sin\varphi)zd\varphi dz. \tag{3.11}$$

Equation (3.8) results now after the change of variables $\varphi' = \varphi+\pi$ in the right-hand side term of (3.11) and from proposition 3.1. □

As a consequence, the projections $\mathscr{P}_{\tau,\delta}$ may be calculated by either of the equations

$$\mathscr{P}_{\tau,\delta} = \mathscr{R}_{\delta+\frac{\pi}{2}}\mathscr{C}_{\alpha,\delta,\beta} \tag{3.12}$$

and

$$\mathscr{P}_{\tau,\delta} = \mathscr{R}_{\delta+\frac{\pi}{2}}\mathscr{C}_{\alpha,\delta+\pi,\beta}, \tag{3.13}$$

for α,β chosen such as $b(\alpha,\beta)=\tau$. Thus the projections $\mathscr{C}_{\alpha,\delta+\pi,\beta}$ and $\mathscr{C}_{\alpha,\delta,\beta}$ share the same information required by the $\mathscr{P}$ transform.

4. The inverse $\mathscr{P}$ transform

We will show now that the function f may be computed as soon as all its projections $\mathscr{P}_{\tau,\delta}$ are available, for $\tau\geq 0$ and $\delta\in[0,\pi)$.

Theorem 4.1. *The $\mathscr{P}$ transform is invertible, meaning that any function $f\in\mathscr{S}(\mathbb{R}^3)$ may be calculated from its $\mathscr{P}$ projections as:*

$$\begin{aligned}f(x,y,z) &= 2\pi\int_0^{\pi}\int_{-\infty}^{\infty}\left(\int_0^{\infty}\widehat{\mathscr{P}_{\tau,\delta}f}(\rho)J_0(2\pi z\tau\rho)d\tau\right) \\ &\qquad\times e^{2i\pi\rho(-x\sin\delta+y\cos\delta)}|\rho|^3 d\rho d\delta.\end{aligned} \tag{4.1}$$

Proof. Taking the Fourier transform of $\mathscr{P}_{\tau,\delta}f$ from (3.6) leads, for all $\rho\in\mathbb{R}$, to

$$\widehat{\mathscr{P}_{\tau,\delta}f}(\rho) = 2\pi\tau\int_0^{+\infty}\widehat{\mathscr{R}_{\delta+\frac{\pi}{2}}f_z}(\rho)J_0(2\pi z\tau\rho)zdz, \tag{4.2}$$

where J_0 is the zero-order Bessel function of first kind. By the projection-slice theorem, the Fourier transform of the Radon projection $\mathscr{R}_{\delta+\frac{\pi}{2}} f_z$ may be replaced by a line from the two-dimensional Fourier transform of f_z and equation (4.2) becomes:

$$\widehat{\mathscr{P}_{\tau,\delta} f}(\rho) = 2\pi\tau \int_0^{+\infty} \widehat{f_z}(\rho d_2) J_0(2\pi z\tau\rho) z dz. \tag{4.3}$$

On the right hand side one can recognize the Hankel transform of the function $z \mapsto \widehat{f_z}(\rho d_2)$ at a point $\tau\rho$. The Hankel transform being invertible, for some given δ and ρ and for any $z > 0$ we get:

$$\begin{aligned} \widehat{f_z}(\rho d_2) &= 2\pi \int_0^{+\infty} \frac{1}{\tau} \widehat{\mathscr{P}_{\tau,\delta} f}(\rho) J_0(2\pi z\tau\rho) \tau\rho d(\tau\rho) \\ &= 2\pi\rho^2 \int_0^{+\infty} \widehat{\mathscr{P}_{\tau,\delta} f}(\rho) J_0(2\pi z\tau\rho) d\tau. \end{aligned} \tag{4.4}$$

The expression of the two-dimensional inverse Fourier transform in polar coordinates may be written as:

$$f_z(x,y) = \int_0^{\pi} \int_{-\infty}^{\infty} \widehat{f_z}(\rho d_2) e^{2i\pi\rho(-x\sin\delta + y\cos\delta)} |\rho| d\rho d\delta. \tag{4.5}$$

Since $f(x,y,z) = f_z(x,y)$, the expression of f may then be obtained immediately from (4.4) and (4.5). □

The inversion formula for the Compton transform is now straight forward:

Theorem 4.2. *Let f be a function from $\mathscr{S}(\mathbb{R}^3)$. Suppose that for each $\tau \geq 0$ and $\delta \in [0,\pi)$ there is a triple*

$$\begin{aligned} (\overline{\alpha},\overline{\beta},\overline{\delta}) \in \Big\{ (\alpha',\beta',\delta') \in \Big[0,\frac{\pi}{2}\Big) \times \Big[0,\frac{\pi}{2}\Big) \times \mathbb{R} \;\Big|\; \alpha'+\beta' < \frac{\pi}{2}\,, \\ b(\alpha,\beta) = \tau,\ \delta' \equiv \delta\,[\pi] \Big\}\,, \end{aligned} \tag{4.6}$$

such that the Compton projection $\mathscr{C}_{\alpha',\delta',\beta'}$ is known. Then the function f may be uniquely found from (4.1)*, where $\mathscr{P}_{\tau,\delta}$ should be replaced with $\mathscr{R}_{\delta+\frac{\pi}{2}} \mathscr{C}_{\alpha',\delta',\beta'}$.*

Theorem 4.2 shows that the inversion of the Compton transform may be done from only projections bellonging to some proper subsets of the set of Compton projections. In this sense we say that the Compton transform is redundant. However, in each subset there are projections that may not be measured with a finite extent planar camera. Indeed, for large enough values of α, Compton cones that intersect the source have the apex $u = (x_1, y_1, 0)$ out of the detector, thus $\mathscr{C}_{\alpha,\delta,\beta}(u)$ is not acquired.

5. Numerical results

The proposed method was tested on Monte-Carlo simulated data. Simulations were performed using Cosima, a Monte-Carlo tool based on Geant4 [1] (version 9.5), which is part of the MEGAlib package [15]. The Geant4 Livermore package was used for electromagnetic interactions and the standard QGSP-BIC-HP physics list for hadronic interactions.

The simulated Compton camera is composed of a stack of three double-sided Silicon-strip scatter detectors and an absorber composed of 64×64 CsI crystals. Each strip detector is made of 3×3 wafers of size 6.3×6.3 cm^2, for a total size of 19.4×19.4 cm^2. Each wafer contains 128×128 strips. A uniform 1-sigma energy resolution of 1 keV and a 10 keV threshold were assumed in the scatterer.

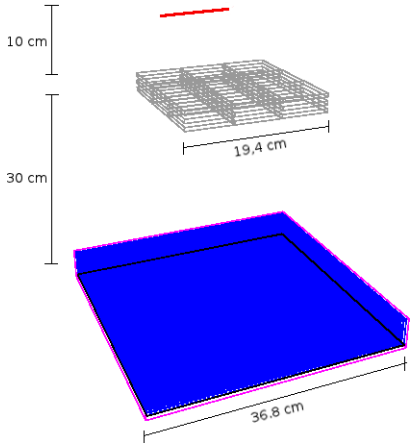

Figure 4. Geometry setup of the experiment.

The elements of the absorber are $0.5 \times 0.5 \times 2$ cm^3 bars. The total size of the absorber is $36.8 \times 36.8 \times 2$ cm^3. A 1-sigma energy resolution of 9.3 keV at 364 keV and a threshold of 20 keV were assumed. For an event to be triggered at least one hit in the scatterer and one hit in the absorber were required. The distance between the lower layer of the scatterer and the absorber is 30 cm and the distance between two consecutive layers of the scatterer is 1 cm (see figure 4).

A line source of γ particles having energies of 364 keV was simulated. The line segment has the extremities in, respectively, $(0, -11, 0)$ cm (out of the vertical parallelepiped having the scatterer as base) and $(0, 0, 0)$ cm (situated on the normal to the camera at its center).

The simulation was run until a number of 8.25×10^5 triggered events was reached. From them, 5.3×10^5 were selected for the reconstruction algorithm, as having Compton cones of parameters $\alpha, \beta \in [0, \pi/2)$ that also

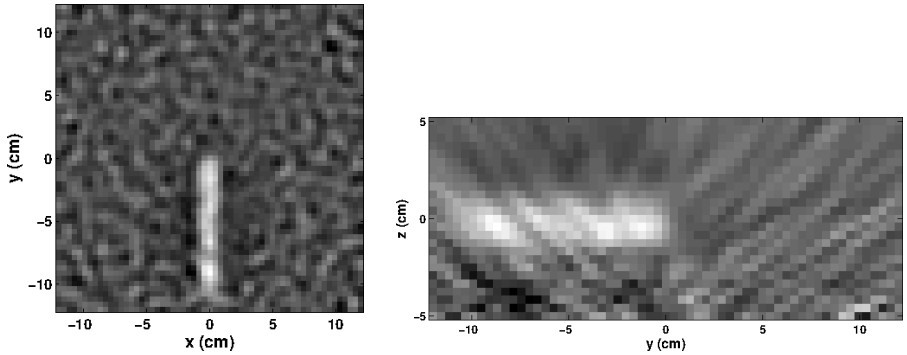

(a) (b)

Figure 5: Line source, with extremities at $(0, -11, 0)$ and $(0, 0, 0)$. A slice parallel to the camera at altitude $z = 0$ cm is shown in (a). The dimensions of the image are 24×24 cm^2. The extremities of the line source may be correctly identified on the reconstructed image. In (b), a slice orthogonal to the camera is shown. It may be noted that the resolution of the image in the vertical direction is sensibly worst than in directions parallel to the camera.

satisfy the constraint $\alpha + \beta < \pi/2$. A five-dimensional table was created by binning the measured events according to the values of the parameters $\alpha, \delta, \beta, x_1$ and x_2, corresponding to the set of Compton projections $\mathscr{C}_{\alpha,\delta,\beta}$. From them, the $\mathscr{P}$ projections were calculated. The empirical projections $\mathscr{P}_{\tau,\delta}$ corresponding, by virtue of proposition 3.2 and lemma 3.1, to identical theoretical projections were averaged together.

A three-dimensional image of the source was reconstructed, one slice parallel to the camera at a time, with Matlab. The size of the entire volume is $24 \times 24 \times 10$ cm^3. Two central slices from the volume are shown in figure 5, one parallel to the camera and one orthogonal to it. In both images, the size of a pixel is 0.4×0.4 cm^2. It may be noted that the resolution in the plane parallel to the camera is better that in the plane orthogonal to it. Some star-shaped artifacts recalling X-ray computed tomography may be observed. The absence of measures in some projections explain the elongation of the source in the z direction and also its displacement towards the detector, artifacts that may be observed in figure 5 (b). For the same reason, more the source point is close to the azimuth of the camera, better it is reconstructed. The central extremity of the line source may be recovered with a very good precision.

6. Conclusions

We proposed a method for the inversion of the Compton transform to be used in tomographical reconstruction of Compton camera images. We shown that there are classes of Compton projections that are related together. Projections from the same class may equally be employed in the reconstruction process or averaged for better the signal-to-noise ratio. However, for a finite size camera, most projections are truncated or even not measured. A selection of (less truncated) measures may be useful in practice. The finite size of the camera has an impact especially the orthogonal direction. Smaller the camera, closer to the detector and elongated appears to be the source.

Analytic algorithms are deemed to be fast in tomographic reconstruction. They need relatively small memory amount and calculation time compared to their iterative counterparts. Also, they do not require often untractable calculation of normalisation factors and their results are not dependent on the choice of the number of iteration steps. These reasons made analytical methods quantitative, meaning that the activity of the source may be related by some proportionality factor to the values in the reconstructed image. However, in Compton camera imaging with a finite extent detector, projection truncation is a key issue that should be addressed in order to allow quantitative imaging.

Acknowledgments

This research is supported by the ENVISION project (co-funded by the European Commission under the FP7 Collaborative Projects Grant Agreement Nr. 241851FP7), by the ETOILE Research Program (PRRH/UCBL, under CPER 2007-13 funding) and by LabEx PRIMES.

References

[1] S. Agostinelli *et al.*, Geant4-A simulation toolkit, *Nucl. Instrum. Methods A*, **506** (2003), 205-303.

[2] M.S. Bandstra *et al.*, Detection and imaging of the Crab nebula with the nuclear Compton telescope, *The Astrophysical Journal*, **738**, *1* (2011), 1-8.

[3] R. Basko, G. L. Zeng and G. T. Gullberg, Application of spherical harmonics to image reconstruction for the Compton camera, *Phys. Med. Biol.*, **43** (1998), 887-894.

[4] M.J. Cree and P.J. Bones, Towards direct reconstruction from a gamma camera based on Compton scattering, *IEEE Transactions on Medical Imaging*, **13**, *2* (1994), 398-407.

[5] M. Frandes, A. Zoglauer, V. Maxim and R. Prost, A tracking Compton-scattering imaging system for hadron therapy monitoring, *IEEE Transactions on Nuclear Science*, **57**, *1* (2010), 144-150.

[6] L. Han, W.L. Rogers, S. S. Huh and N. Clinthorne, Statistical performance evaluation and comparison of a Compton medical imaging system and a collimated

Anger camera for higher energy photon imaging, *Phys. Med. Biol.*, **53**, *24* (2008), 7029-7045.

[7] M. HIRASAWA and T. TOMITANI, An analytical image reconstruction algorithm to compensate for scattering angle broadening in Compton cameras, *Phys. Med. Biol.*, **48** (2003), 1009-1026.

[8] W. LEE and T. LEE, A compact Compton camera using scintillators for the investigation of nuclear materials, *Nucl. Instrum. Methods A*, **624** (2010), 118-124.

[9] X. LOJACONO, V. MAXIM, A. ZOGLAUER, F. PEYRIN and R. PROST, *A filtered backprojection reconstruction algorithm for Compton camera*, in Fully 3D, pp. 96-99, 2011.

[10] V. MAXIM, M. FRANDES and R. PROST, Analytical inversion of the Compton transform using the full set of available projections, *Inverse Problems*, **25**, *9* (2009), 1-21.

[11] L.C. PARRA, Reconstruction of cone-beam projections from Compton scattered data, *IEEE Transactions on Nuclear Science*, **47**, *4* (2000), 1543-1550.

[12] B. SMITH, Reconstruction methods and completeness conditions for two Compton data models, *J. Opt. Soc. Am. A*, **22**, *3* (2005), 445-459.

[13] B. SMITH, Line-reconstruction from Compton cameras: data sets and a camera design, *Optical Engineering*, **50**, *5* (2011), 1-11.

[14] R. TODD, J. NIGHTINGALE and D. EVERETT, A proposed Gamma camera, *Nature*, **251** (1974), 132-134.

[15] A. ZOGLAUER, R. ANDRITSCHKE and F. SCHOPPER, MEGAlib–The medium energy gamma-ray astronomy library, *New Astron. Rev.*, **50** (2006), 629-632.

Voichita Maxim
Université de Lyon, CREATIS; CNRS UMR5220; Inserm U1044; INSA-Lyon; Université Lyon 1, France
Btiment Blaise Pascal, 7, avenue Jean Capelle, 69621 Villeurbanne cedex FRANCE
E-mail: `voichita.maxim@creatis.insa-lyon.fr`